Microstructure Evolution During the Sintering of Freeze-Cast Alumina

Daniel D. Athayde[a,b]* , Luiz F.S. Lima[a], Peter G. Weidler[c], Alysson Martins Almeida Silva[a],

Wander L. Vasconcelos[d]

[a]*Universidade de Brasília, Faculdade de Tecnologia, Departamento de Engenharia Mecânica, Campus Universitário Darcy Ribeiro, Brasília, DF, Brasil.*
[b]*Universidade Federal de Minas Gerais, Departamento de Engenharia Química, Belo Horizonte, MG, Brasil.*
[c]*Karlsruhe Institute of Technology, Institute of Functional Interfaces, Hermann-von-Helmholtz-Platz 1, 76344, Eggenstein-Leopoldshafen, Germany.*
[d]*Universidade Federal de Minas Gerais, Departamento de Engenharia Metalúrgica e de Materiais, Belo Horizonte, MG, Brasil.*

Reports on freeze-cast ceramic materials frequently focus on the study of the organized macroporosity and the properties of the materials. This study aims to describe the microstructure evolution of freeze-cast alumina during the sintering process, analyzing grain growth, densification, pore elimination and crystal structure at different sintering temperatures (1300-1500 °C). Aqueous suspensions with 20 vol% alumina were freeze-cast in liquid N_2 and sintered. The microstructure was analyzed by stereological analysis, N_2 adsorption and X-ray diffraction. Grain sizes varied within 237-500 nm, and the intergranular porosity decreased from 8.8% at 1300 °C to 1.4% at 1500 °C. N_2 isotherm analysis revealed pore shrinking from the region of macro and mesopores (20-80 nm), to smaller residual mesopores (3.7-15 nm) at temperatures above 1400 °C. Rietveld refinement of the XRD diffractograms confirmed increased crystallite size and decreased lattice strain at higher sintering temperatures. This comprehensive description of microstructural evolution of the freeze-cast alumina contributes to understanding the sintering of highly porous ceramics produced via freeze-casting.

Keywords: *Sintering; freeze-casting; alumina; microstructure.*

1. Introduction

The freeze-casting method has been extensively used in the last two decades for manufacture of materials with organized pore structure[1,2]. Although this technique can be used for manufacturing polymers, biomacromolecules, pharmaceuticals and food-related materials[3], the main focus of materials scientists and engineers has been on developing inorganic materials, namely ceramics[4,5] and metals[6]. The anisotropic pore structure obtained by the freeze-casting method, which depends strongly on the solvent and the conditions during the freezing stage[1,7], is interesting for a wide variety of applications. For instance, highly anisotropic freeze-cast materials have been explored for development of biomimetic materials[8-10] and biomaterials[11,12]. Other applications focused on the high connectivity and tortuosity of macropores in freeze-cast materials for mass transport processes[13], such as membrane manufacture[14-17]. The use of these materials for fuel cell electrodes has also been demonstrated[13,18].

Among the materials commonly used for production of freeze-cast ceramics, alumina (Al_2O_3) is frequently chosen[19-23], since it is a well-known material with several established and mature processing techniques[24]. Alumina also has high melting temperature and chemical stability, as well as high mechanical strength and electrical resistance. These properties have driven the widespread commercial use of alumina for materials that are submitted to high temperatures, and for manufacture of catalyst substrates, electrical insulators and biomaterials[24]. Moreover, several recent studies can be found on novel methods for alumina processing and innovative applications, confirming this as one of the most used oxides for production of ceramic materials[25,26].

Alumina processing is typically performed by a shape-forming stage, such as pressing[27], slip casting[28], extrusion[29] and freeze-casting[1], that forms a porous compact (within 25-60 vol% porosity depending on the process[30]) also known as green body. Then, the shaped ceramic is followed by densification at high temperatures in order to obtain a material with the desired microstructure[31]. The densification stage, also referred as sintering, usually intends to eliminate undesired porosity (e.g. intergranular) and to obtain the proper grain size[32]. The solid-state sintering, which is the commonly used sintering category for alumina powder processing, typically reaches 0.5-0.9 of the alumina melting temperature, providing the required energy for atomic diffusion, which enables particles to join and simultaneously reduces the porosity[32]. These high temperatures also cause grain growth and changes in the pore size distribution[30].

*e-mail: ddathayde@gmail.com

The final material is a strong and dense ceramic presenting the designed properties for the application.

The driving force of solid-state sintering is the reduction in surface free energy, which requires transport of matter, such as atoms, ions and molecules in crystalline solids[32]. Many authors describe the sintering of ceramic materials in three different stages involving particle bonding, densification and grain growth[30,32,33]. In the initial stage, in the region where two or more particles are in contact, the interparticle neck begins to form with less than one-third of the particle size. This stage is usually associated with small dimensional changes (less than 3% shrinkage). Then, in the intermediate stage, the neck growth takes place, resulting in significant densification (if the system allows densification). The pores typically acquire a tubular geometry and remain connected to the external surface, also known as open porosity. Moreover, grains become more spherical, due to the transport of matter, and grain growth starts. The final sintering stage is attributed to intense grain growth and pore separation, involving the formation of residual isolated porosity (not connected to the external surface). The slow densification in the last stage depends on the success of eliminating the isolated pores[33]. It is worth noticing that the rate of each stage strongly depends on the temperature used in the sintering process, since atomic motion increases with temperature[34,35].

The mechanisms involved in the sintering of crystalline materials are typically described as six different paths: vapor transport (evaporation/condensation), surface diffusion, lattice diffusion from the surface, lattice diffusion from the grain boundary, grain boundary diffusion and plastic flow[36,37]. The mechanisms that dominate the sintering process determine if mainly neck growth and particle coarsening will occur (vapor transport, surface diffusion and lattice diffusion from the surface), or if the neck growth will take place together with densification (grain boundary diffusion, lattice diffusion from the grain boundary and plastic flow). For ceramic materials, the grain boundary diffusion and lattice diffusion are the main densification mechanisms[32], with several authors reporting that alumina sintering is controlled by grain boundary diffusion[34,38]. Modeling of the alumina sintering is typically performed focusing on the three stages of the sintering process, and the main kinetic models have been detailed by Zeng et al.[38].

Characterization of sintered Al_2O_3 has been extensively explored by many techniques[19-21,24,34,39]. In addition, many papers have explored the influence of sintering methods and parameters on the final properties of porous alumina ceramics, as well as the microstructure influence on these properties[40-43]. However, there is a lack of studies analyzing the sintering of freeze-cast alumina, although the use of freeze pressing has already been reported for aqueous alumina suspension by Zheng et al.[44]. The results showed that the water freezing generated significant internal forces (comparable to hundreds of MPa) and led to green body densities higher than for alumina ceramic obtained by tape-casting. The implications of the "internal compaction" method, as named by the authors, shifted the initial sintering temperature and changed the shrinkage kinetics[44]. Despite the interesting results on freeze pressing of alumina, it is worth mentioning that the conditions used during the freeze-casting method are quite different, as in most cases the mold is open to the atmosphere or the suspension-air interface is allowed to move freely. Therefore, the internal forces that arise during freeze pressing may be significantly higher than the forces established during freeze-casting.

Another interesting aspect of the freeze-casting method is the concept of a breakthrough concentration that was developed by Shanti et al.[45] and further explored by Deville and Bernard-Granger[46]. This concept is related to the solidification of the solvent during freeze-casting, in which the solid (frozen solvent) and liquid (ceramic suspension) interface in the advancing freezing front firstly push the alumina particles forming the organized macropores. As the alumina particle concentration increases between the freezing fronts, there is a moment when the capillary drag force pushing the particles in the solid/liquid interface balances with osmotic pressure due to the particle concentration. The concentration at which the osmotic pressure exceeds the capillary pressure is the breakthrough concentration, resulting in the solid/liquid interface entering the interparticle space and forming interparticle porosity[45,46]. Therefore, the production of freeze-cast substrates with organized pore structure produces a final material that typically is a highly porous material with large anisotropic macropores[21] and smaller interparticle porosity. In this context, the particle coalescence, grain growth, densification and pore elimination may differ from other moulding and sintering methods.

Therefore, this study aims to evaluate the sintering process on freeze-cast alumina substrates and compare the results from different characterization methods, such as stereological analysis of SEM micrographs, N_2 adsorption and X-ray diffraction analysis. Since the macroporosity and the mechanical behavior of the alumina freeze-cast substrate produced in this study has already been described elsewhere[21,47], this report focuses mainly on the interparticle porosity, as well as the effects of sintering temperature on the crystallite size and lattice strain. The N_2 adsorption isotherms were analyzed using both the BET/classical and DFT methods, allowing estimation of the presence of pores and pore size distribution. Regarding XRD, the diffractograms were investigated by Rietveld refinement. Finally, a comparison of the characterization methods was performed in order to describe the microstructure development of the freeze-cast alumina tubes.

2. Materials and Methods

The tubular alumina substrates were produced by the freeze-casting method and described elsewhere[21]. In summary, alumina powder (Almatis – CT 3000 SG, D_{50} = 500 nm) were added to an aqueous solution with 2% (wt%) sodium polyacrylate (Sigma-Aldrich) as dispersant and polyvinyl alcohol (Sigma-Aldrich) as a binder. The aqueous suspension further explored in this study was produced with 20 vol% alumina. The mixture was mixed for 24 h, followed by 10 min ultrasound bath to eliminate air bubbles. Then, the aqueous solution was poured dropwise inside a copper tubular mold (dimensions can be found in Athayde et al.[21]) and immersed in liquid nitrogen for 30 s. The substrates were manually withdrawn, placed inside a freeze-dryer for 24 h and sintered (Thermolab – Thermocouple Pt30%Rh/

Pt6%Rh) at 1300-1500 °C for 1 h with heating and cooling rates of 2 °C.min^{-1}. The final alumina ceramics were obtained in tubular geometry with external and internal diameter varying, respectively, within 10.7-11.9 mm and 6.6-7.6 mm (depending on the sintering temperature). Average length of the tubes was 45.0 mm.

Stereological measurements were performed with the ImageJ software using five different SEM micrographs (using a Quanta FEG 3D FEI microscope) for each sintering temperature for estimating the grain size, intergranular porosity (in %) and intergranular pore size[48,49]. The N_2 adsorption tests were performed in a Quantachrome Autosorb 1C equipment, and the obtained isotherms were analyzed by BET (Brunauer-Emmet-Teller); whereas the porosity was assessed using the Kelvin-equation and DFT (Density Functional Theory) methods[50,51]. In addition, a comparative N_2 adsorption analysis was performed (model-free comparison plot), in which the isotherm points for the commercial alumina powder were used as a reference and all the other isotherms were plotted against the alumina powder (called "original powder" henceforth).

For BET analysis, a rough estimation of the mean particle diameter, considering spherical particles, was performed using Equation 1[52]:

$$d_{BET} = \frac{6000}{A_{BET}\rho} \qquad \text{Eq. 1}$$

where d_{BET} is the mean particle diameter (nm), A_{BET} is the BET specific surface area (SSA) (m[2].g[-1]) and ρ is the theoretical specific mass of alumina (3.94 g.cm^{-3}). Regarding the DFT method, the model with the best fit was chosen and applied to all samples using adequate pore geometry. In this study the DFT model was based on cylindrical pores, because the pores are elongated, using the NLDFT (non-local density functional theory) adsorption branch, and N_2 at 77 K on silica.

The X-ray diffraction (XRD) analysis was performed at room temperature using a Philips-Panalytical PW 1710 diffractometer, with Cu Kα radiation and operating at 40 kV and 40 mA. The scan was performed over an angular range between 3.03° and 89.97° 2θ, with a scan step size of 0.060° 2θ and scan step time of 1 s. The diffractograms were analyzed using the TOPAS V6 software[53,54]. For estimation of the crystallite size (i.e. coherence length) and the lattice strain, the Rietveld refinement method and the TCHZ-pseudo-Voigt profile function (Thompson-Cox-Hastings[55]) was applied. This approach considers contribution from the crystallite size and stress/strain effects on broadening of the lines. Structural data was obtained from the COD, the Crystal Open Database[56].

3. Results and Discussion

The alumina freeze-cast tubes produced in this study have already been reported in previous studies describing the structure of the macropores produced by freeze-casting and its influence on the mechanical behavior[21,47], as well as for production of membranes[14,57]. Representative micrographs of the radially aligned porosity are reproduced for reader's ease in Figure 1a, with pore sizes ranging within 5-10 µm[57]. The microstructure exhibiting the grains after sintering is also reproduced in Figure 1b, c for each sintering temperature used in this study, with average grain sizes of 237±44 nm, 250±34 nm and 500±105 nm for the samples sintered at 1300 °C, 1400 °C and 1500 °C, respectively[21].

Alongside the grain size estimation, the stereological analysis allowed estimation of the intergranular porosity as well as the intergranular pore size by measuring the void spaces between the particles (Figure 1b-d). These results are shown in Table 1 and will be compared with the concept of breakthrough concentration. In this study all samples were prepared with the same solidification procedure (immersed in liquid N_2) and using similar solid concentrations of the initial slurry (20 vol%).
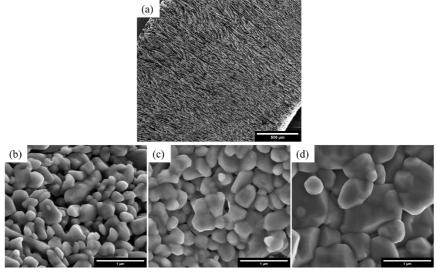

Figure 1. Representative SEM micrographs of the freeze-cast tubular substrates showing (a) the radially aligned macropores (scale bar 500 µm)[57], and the microstructures of the sintered alumina at (b) 1300 °C, (c) 1400 °C and (d) 1500 °C (scale bar 1 µm)[21]. Reproduced with permission[57] under Creative Commons Attribution License. Reproduced with permission[21]. Copyright 2020, John Wiley and Sons.

Therefore, the breakthrough concentration did not vary among the produced samples as it depends on the temperature, the surface tension of the solvent and particle radius[46]. According to Deville and Bernard-Granger[46], if a maximum solid concentration of 0.64 is assumed (when the osmotic pressure becomes infinite[45]) an aqueous slurry of ceramic particles exhibits a breakthrough concentration of 0.63. This value reveals that the initial solid concentration of the green body was 63% (in volume), which expresses the initial packing for densification during the sintering process of the freeze-cast ceramic, and the initial intergranular porosity was 37% (in volume).

The results in Table 1 showed that the intergranular porosity decreases to values of 8.8% for the sample sintered at 1300 °C, revealing initial pore elimination. At this temperature, it is already possible to notice a small degree of particle bonding by the formation of necks where the particles are in contact. However, further analysis of Figure 1b revealed a great amount of pores within the particles, thus explaining the high 8.8% intergranular porosity. As the sintering temperature increases to 1400 °C, the porosity decreased considerably to 3.4%. The intense increase of the neck is visible, forming a coarsened structure. A further increase of the sintering temperature to 1500 °C resulted in a densified structure with larger grains, while maintaining only a small amount of pores between grains. The residual intergranular porosity by the stereological method was 1.4%, which indicates 96% pore elimination when compared to the breakthrough concentration. Meanwhile, the development of the microstructure significantly impacted the intergranular pore diameter, as shown in Table 1. Despite the large experimental errors associated with the estimated values

by this method, it is possible to notice a decrease from the 192 nm intergranular pores when sintered at 1300 °C to the 90 nm pore diameter at 1500 °C.

Regarding the N_2 adsorption, the isotherms are shown in Figure 2. All the samples in Figure 2a display the typical behavior of a Type II isotherm according to the IUPAC classification of physisorption isotherms[58]. These are typical of macroporous materials, which indeed is the aim of the freeze-cast method for production of aligned macroporosity[4]. The knees of the curves found for the samples at low P/P_0 are typically attributed to the formation of a monolayer, followed by the linear section of the isotherms at intermediate values of P/P_0. This knee is more distinct for the original powder and its curvature becomes less pronounced as the sintering temperature increases from 1300 °C to 1500 °C. The shape of the isotherms shows soaking of the material by nitrogen pore condensation, as the adsorbed volume increases significantly due to pores larger than 100 nm when P/P_0 reaches values closer to unity. Hysteresis was found only for the sample sintered at 1400 °C, suggesting the development of bottlenecks on the intergranular pores. The comparative plot at Figure 2b was used to examine the effect of the sintering process on the alumina substrates in comparison to the commercial alumina powder. Clearly the samples adsorbed much less N_2 molecules than the original powder, mainly in the lower relative pressures (P/P_0) range and close to saturation pressure.

The BET specific surface areas, as well as a rough estimate of the spherical particle diameter by Equation 1, were reported in Table 2. As expected, a trend of decrease on the specific surface area and in the particle size was found as the sintering temperature increases.

Table 1. Results obtained by stereological methods for the microstructures of the sintered samples shown in Figure 1b-d. At least 5 SEM micrographs were used for each sample for the stereological analysis.

Sintering temperature (°C)	Intergranular porosity (%)	Intergranular pore diameters (nm)
1300	8.8 ± 3.6	192 ± 150
1400	3.4 ± 2.6	152 ± 125
1500	1.4 ± 0.8	90 ± 55

(a)   (b)
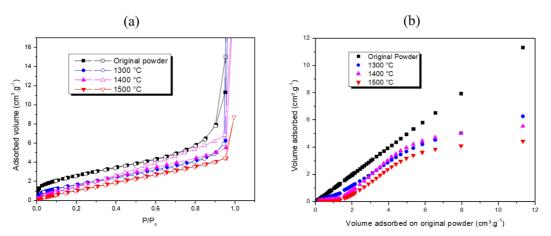

Figure 2. N_2 adsorption analysis detailing (a) the adsorbed volume, and (b) comparative curves using the original powder as comparison. Solid points represent adsorption whereas hollow points represent desorption.

Only the sample sintered at 1400 °C did not follow this trend as they showed an increase of the specific surface area from 6.9 to 7.7 $m^2.g^{-1}$ when the temperature was increased from 1300 °C to 1400 °C. Although the BET model errors (determined from one isotherm and listed in Table 2) were small, the isotherms for these two samples (sintered at 1300 °C and 1400 °C – Figure 2) are almost the same, explaining the observed minor difference in SSA. Specific pore volume (calculated at P/P_0 around 0.99 and corresponding to pore diameters of up to approximately 300 nm) showed a trend of decreased pore volume with sintering at higher temperatures. It was observed a significant decrease from 0.153 $cm^3.g^{-1}$ to 0.014 $cm^3.g^{-1}$ for the sample sintered at 1500 °C, confirming elimination of more than 90% of the pore volume as the sintering takes place.

The N_2 adsorption isotherms were also explored using the DFT method, with the resulting pore size distribution curves shown in Figure 3. Both the commercial powder and the alumina tube sintered at 1300 °C presented similar pore size distribution at the mesopore and macropore ranges, with pores varying within 20-80 nm. The modal pore size, detailed in Table 2, varied from 29.4 nm for the powder to 30.4 nm for the sintered alumina, indicating possible pore coalescence by the sintering at 1300 °C. Moreover, this sintering temperature resulted in a decrease on the specific pore volume significantly from 0.121 $cm^3.g^{-1}$ to 0.073 $cm^3.g^{-1}$, an elimination of roughly 40% of the initial porosity. Further increase of the sintering temperature to 1400 °C resulted in the development of a smaller population of mesopores in the range within 3.7-15.0 nm. The presence of these pores decreased the modal pore diameter to 4.9 nm. The larger pores within 20-80 nm are still present, though with much lower contribution to the total pore volume, as depicted in Figure 3. The trend of decreased specific pore volume by DFT was similar to the trend estimated by the specific pore volume, with an elimination of 77% of the porosity, compared to the original powder. Finally, the freeze-cast alumina sintered at 1500 °C decreased even further the contribution of the larger pores, with a specific pore volume of 0.012 $cm^3.g^{-1}$ and elimination of 90% of the porosity. The modal pore size did not vary from the sample sintered at 1400 °C and the value was kept at 4.9 nm.

The sintering behavior of the freeze-cast alumina tubes can be correlated with the well-known microstructure development during solid-state sintering. For instance, the pore coalescence at the intermediate stages of sintering usually results in an increase of the mean pore size. Meanwhile, the formation and increase of the interparticle necks leads to the formation of a tubular pore network. Both phenomena were found for the sample sintered at 1300 °C when compared to the commercial alumina, as the pore size slightly increased and the fitting error of the DFT method (based on cylindrical pores) was the lowest obtained in this study. As the sintering goes to the final stages, pore elongation and thinning take place, up to the point where the pores pinch off and form closed spherical pores, also known as pore closure[33]. This was observed for the sample sintered at 1400 °C and 1500 °C, as smaller pores were found, whereas the larger pores within 20-80 nm were gradually eliminated. The appearance of smaller pores due to the formation of spherical pores was in accordance to the hysteresis found for the sample sintered at 1400 °C. The largest value of pore elimination of 90% after sintering at 1500 °C without further decrease on the modal pore diameter suggests that the smaller mesopores (3.7-15.0 nm) will probably be retained at the final structure and will account for the residual porosity, whereas the larger pores will be extinguished. Finally, the decrease in specific pore area as the sintering advanced was also found, which is expected by the sintering mechanism.

The XRD diffractograms for all samples are depicted in Figure 4, all peaks from the 4 diffractograms were attributed to the Al_2O_3 phase (ICSD collection code 031545). An overall behavior found was the shift of the peak center to higher 2θ values as the sintering temperature increases, whereas the IB (integral breadth) decreases, but leveling out for the sample sintered at 1500 °C. The results from the Rietveld refinement are shown in Table 3, detailing the cell parameters and cell volume of the alumina samples.
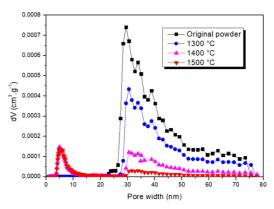

Figure 3. Pore size distribution of the original powder and the sintered samples, data calculated by the DFT method.

Table 2. Results from the N_2 adsorption analysis, comparing BET and DFT analysis. Specific pore volume was calculated at P/P_0 around 0.99 and at maximum point of P/P_0 for DFT analysis (maximum pore diameter of 78 nm calculated by DFT).

Sintering temperature (°C)	BET & pore analysis			DFT analysis			
	Specific surface area ($m^2.g^{-1}$)	Mean spherical particle diameter (Equation 1) (nm)	Specific pore volume ($cm^3.g^{-1}$)	Modal pore diameter (nm)	Specific pore volume ($cm^3.g^{-1}$)	Specific pore area ($m^2.g^{-1}$)	Fitting error (%)
Original powder	9.9 ± 0.3	154.2	0.153	29.4	0.121	12.4	3.79
1300	6.9 ± 0.4	221.6	0.093	30.4	0.073	7.2	1.95
1400	7.7 ± 0.5	197.5	0.034	4.9	0.028	5.5	3.71
1500	6.2 ± 0.3	244.6	0.014	4.9	0.012	4.0	5.66

The commercial alumina exhibited a crystallite size of 102.3 nm, with a slight decrease to 81.6 nm for the sample sintered at 1300 °C. As for the samples sintered at higher temperatures, the crystallite size showed significant increase to 239.8 nm and 261.0 nm for the samples sintered at 1400 °C and 1500 °C, respectively.

It is worth noticing that the crystallite size (Table 3) is in the same order of magnitude of the grain sizes reported (237-500[21] nm), though the crystallite size was always smaller than the grain size. This is in accordance to the theory, as the crystallite size reports the size of single crystals (determined by a coherent diffraction domain in XRD patterns), while the grain size (determined by stereological analysis or granulometry if agglomerates are not found) can be composed of a single crystal or a polycrystalline material[59]. Regarding the lattice strain, also detailed in Table 3, it showed considerable decrease as higher sintering temperatures were used. The original powder presented lattice strain of 0.00044 and the sintered samples exhibited 0.00013, 0.00008 and 0.00003 when sintered at 1300 °C, 1400 °C and 1500 °C, respectively.

Estimates of the crystallite sizes and lattice strains were plotted in Figure 5, together with the curves showing the overall behavior of both parameters with the sintering temperature. The crystallite size for the sample sintered at 1300 °C shown in Figure 5 indicates that there is an onset temperature to start the sintering process involving grain growth. For the alumina samples in this study, only at 1400 °C the system contained enough energy for the mass transport phenomena for the sintering process, resulting in crystallite size increase. Overall, the crystallite size of the sample sintered at 1500 °C increased 155% in comparison with the original powder. This is accordance to the grain growth observed for the freeze-cast alumina tubes (Figure 1) estimated at 110% for the same comparison[21], since higher sintering temperature promotes higher crystallite size due to the higher diffusion rates of the ions[60], as shown by Equation 2[33,36]:

$$D_V = D_0 exp\left(-\frac{Q}{RT}\right) \qquad \text{Eq. 2}$$

where D_V is the volume diffusion coefficient, D_0 is the pre-exponential factor, Q is the activation energy, R the universal gas constant and T the temperature. Regarding the lattice strain shown in Figure 5, the Rietveld refinement estimated the decrease on lattice deformation for higher temperatures, indicating decrease of lattice deformation at higher temperatures due to lower distortions and crystal imperfections[39].

According to a sintering diagram for alumina reported by Kang and Jung[35], the temperatures used in this study (all lower than 77% of the alumina melting temperature – 2072 °C) were dominantly in the region where the grain-boundary diffusion is the main sintering mechanism. For this mechanism, the densification rate can be calculated by Equation 3[35]:

$$\frac{d\rho}{dt} = \frac{733D_b\delta_b\gamma_s V_m}{RTG^4} \qquad \text{Eq. 3}$$

where ρ is the relative density, t is time, D_b is the grain boundary diffusion coefficient, δ_b is the diffusion thickness of grain-boundary diffusion, V_m the molar volume and G is the grain size. All the values required to use this equation for alumina can be found elsewhere[35].
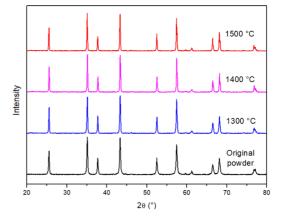

Figure 4. X-ray diffractograms of the original powder and the sintered samples.
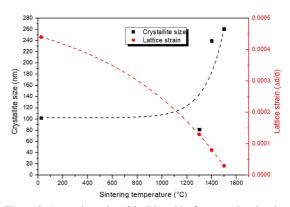

Figure 5. Comparison plot of the Rietveld refinement showing the increase of the crystallite size and decrease on the lattice strain. The dashed curves were schematically plotted to display the overall behavior of these parameters with sintering temperature.

Table 3. Compiled results from the XRD analysis by Rietveld refinement.

Sintering temperature (°C)	Cell parameters (Å)		Cell volume (Å³)	Crystallite size (nm)	Lattice strain Δd/d
	a	c			
Original powder	4.7631	13.0011	255.44	102.3	0.00044
1300	4.7612	12.9981	255.18	81.6	0.00013
1400	4.7603	12.9962	255.04	239.8	0.00008
1500	4.7603	12.9975	255.06	261.0	0.00003

In this study, a comparison of the characterization methods revealed several agreements between the results. For instance, the stereological analysis was accurate on estimating the percentage of the intergranular porosity, as confirmed by the specific pore volume predicted by the BET and DFT methods. Regarding the size distribution of the intergranular pores, the DFT allowed comprehension on the sintering process with elimination of large meso and macropores simultaneous to the formation of smaller mesopores that probably will remain as residual pores due to their stability even when the temperature was increased from 1400 °C to 1500 °C. These phenomena are in accordance to the dominance of the grain boundary diffusion for all the sintering temperatures used in this study as aforementioned. The densification that occurs when this mass diffusion mechanism predominates typically causes grain growth as well as decrease of pore sizes (from 192 nm to 90 nm by the stereological characterization and shift of pore sizes by DFT – Figure 3 – when temperature increased from 1300 °C to 1500 °C). In this mechanism, particles diffuse from the grain boundary to the interparticle voids (interparticle pores), shrinking the pores. Moreover, the grain growth rate is still relatively lower than the pore mobility at this temperature range according to Kang and Jung[35] (with maximum temperature kept only for 1 h) and, hence, there is no formation of pores within the grain as seen in Figure 1c. If there would be a change of sintering mechanism from grain boundary diffusion to lattice diffusion, which typically occurs over 99% of relative density, there would be pore coalescence and increase on pore size, which is not observed in this study.

As for the XRD diffractograms, the overall increase on crystallite size agreed well with the grain size estimation by stereological methods. An analysis of the average number of crystallites in each grain (ratio between average grain volume V_G and average crystallite volume V_D assuming they are spherical[59]) revealed that the sample sintered at 1300 °C showed a V_G / V_D value of 24.5. Meanwhile the sample sintered at 1400 °C revealed a more crystallographic homogeneous structure, reaching a ratio around 1 crystallite per grain. This aligns with the predominant grain boundary diffusion sintering mechanism in this temperature range[59]. A slight increase to 7.0 was found for the sample sintered at the highest temperature (1500 °C), which may indicate a slight degree of lattice diffusion in which the grain growth by this mechanism incorporates new crystallites[59]. Nevertheless, the overall results indicate that the prevailing mechanism is still the grain boundary diffusion, which is in accordance to the used sintering temperatures and the degree of densification of the samples obtained in this study[35].

4. Conclusion

The analysis of the sintering process on the alumina tubes produced by freeze-casting method allowed the exploration of the microstructural evolution of each sintering temperature. SEM micrographs showed that at low sintering temperatures prevails small grains with initial formation of the interparticle neck, with abundance of interparticle pores. As the temperature increases to 1400 °C, the necks begin to grow, followed by intense pore elimination and grain growth at 1500 °C. Results from the N_2 adsorption

revealed similar behavior with decrease of the specific pore volume and surface area by the DFT method, suggesting pore elimination. The larger meso and macropores (20-80 nm) were eliminated with increasing sintering temperature. However, the thinning and elongation of these pores resulted on the pinching off of the intergranular pores and resulted in the formation of small closed pores in the mesopore region (3.7-15 nm) at 1400 °C. In fact, these smaller pores were still found for the sample sintered at 1500 °C, without any noticeable decrease in pore volume at this region. As for the XRD data, an increase of crystallite size and a decrease of lattice strain was found. This is in accordance to the expected behavior during sintering, as higher diffusion rates are found for higher temperatures. A comparison of the results obtained in this study with previous reports revealed that the prevailing sintering mechanism is the grain boundary diffusion. Therefore, the analysis of the microstructure allowed description of the sintering process for the highly porous alumina tubes, which is paramount for understanding the properties and performance of freeze-cast materials.

6. References

1.	Deville S. Freeze-casting of porous ceramics: a review of current achievements and issues. Adv Eng Mater. 2008;10(3):155-69. http://dx.doi.org/10.1002/adem.200700270.

2.	Scotti KL, Dunand DC. Freeze casting: a review of processing, microstructure and properties via the open data repository, FreezeCasting.net. Prog Mater Sci. 2018;94:243-305. http://dx.doi.org/10.1016/j.pmatsci.2018.01.001.

3.	Shao G, Hanaor DAH, Shen X, Gurlo A. Freeze casting: from low-dimensional building blocks to aligned porous structures: a review of novel materials, methods, and applications. Adv Mater. 2020;32(17):1907176. http://dx.doi.org/10.1002/adma.201907176.

4.	Liu R, Xu T, Wang C. A review of fabrication strategies and applications of porous ceramics prepared by freeze-casting method. Ceram Int. 2016;42(2):2907-25. http://dx.doi.org/10.1016/j.ceramint.2015.10.148.

5.	Santos LNRM, Silva JRS, Cartaxo JM, Rodrigues AM, Neves GA, Menezes RR. Freeze-casting applied to ceramic materials: a short review of the influence of processing parameters. Ceramica. 2021;67(381):1-13. http://dx.doi.org/10.1590/0366-69132021673812923.

6.	Jung H, Jang TS, Wang L, Kim HE, Koh YH, Song J. Novel strategy for mechanically tunable and bioactive metal implants. Biomaterials. 2015;37:49-61. http://dx.doi.org/10.1016/j.biomaterials.2014.10.027.

7.	Deville S. Ice-templating, freeze casting: beyond materials processing. J Mater Res. 2016;28(17):2202-19. http://dx.doi.org/10.1557/jmr.2013.105.

8.   Porter MM, Mckittrick J, Meyers MA. Biomimetic materials by freeze casting. J Miner Met Mater Soc. 2013;65(6):720-7. http://dx.doi.org/10.1007/s11837-013-0606-3.

9.   Zhao N, Li M, Gong H, Bai H. Controlling ice formation on gradient wettability surface for high-performance bioinspired materials. Sci Adv. 2020;6(31):1-10. http://dx.doi.org/10.1126/sciadv.abb4712.

10. Bai H, Wang D, Delattre B, Gao W, De Coninck J, Li S, et al. Biomimetic gradient scaffold from ice-templating for self-seeding of cells with capillary effect. Acta Biomater. 2015;20:113-9. http://dx.doi.org/10.1016/j.actbio.2015.04.007.

11. Deville S, Saiz E, Tomsia AP. Freeze casting of hydroxyapatite scaffolds for bone tissue engineering. Biomaterials. 2006;27(32):5480-9. http://dx.doi.org/10.1016/j.biomaterials.2006.06.028.

12. Naleway SE, Fickas KC, Maker YN, Meyers MA, McKittrick J. Reproducibility of ZrO_2-based freeze casting for biomaterials. Mater Sci Eng C. 2016;61:105-12. http://dx.doi.org/10.1016/j.msec.2015.12.012.

13. Lichtner AZ, Jauffrès D, Roussel D, Charlot F, Martin CL, Bordia RK. Dispersion, connectivity and tortuosity of hierarchical porosity composite SOFC cathodes prepared by freeze-casting. J Eur Ceram Soc. 2015;35(2):585-95. http://dx.doi.org/10.1016/j.jeurceramsoc.2014.09.030.

14. Athayde DD, Motuzas J, Diniz da Costa JC, Vasconcelos WL. Novel two-step phase inversion and dry surface coated carbon membranes on alumina freeze-cast substrates for desalination. Desalination. 2021;500:1148620. http://dx.doi.org/10.1016/j.desal.2020.114862.

15. Athayde DD, Souza DF, Silva AMA, Vasconcelos D, Nunes EHM, Diniz da Costa JC, et al. Review of perovskite ceramic synthesis and membrane preparation methods. Ceram Int. 2015;42(6):6555-71.

16. Gaudillere C, Garcia-Fayos J, Plaza J, Serra JM. Ice-templating for the elaboration of oxygen permeation asymmetric tubular membrane with radial oriented porosity. Ceramics. 2019;2(2):246-59. http://dx.doi.org/10.3390/ceramics2020020.

17. Liu T, Lei L, Gu J, Wang Y, Winnubst L, Chen C, et al. Enhanced water desalination performance through hierarchically-structured ceramic membranes. J Eur Ceram Soc. 2017;37(6):2431-8. http://dx.doi.org/10.1016/j.jeurceramsoc.2017.02.001.

18. Panthi D, Hedayat N, Woodson T, Emley BJ, Du Y. Tubular solid oxide fuel cells fabricated by a novel freeze casting method. J Am Ceram Soc. 2020;103(2):878-88. http://dx.doi.org/10.1111/jace.16781.

19. Souza DF, Nunes EHM, Pimenta DS, Vasconcelos DCL, Nascimento JF, Grava W, et al. Synthesis and structural evaluation of freeze-cast porous alumina. Mater Charact. 2014;96:183-95. http://dx.doi.org/10.1016/j.matchar.2014.08.009.

20. Souza DF, Nunes EHM, Queiroga JA, Vasconcelos WL. Microstructural characterization and gas permeation performance of freeze-cast alumina supports. J Eur Ceram Soc. 2018;38(11):4020-5. http://dx.doi.org/10.1016/j.jeurceramsoc.2018.04.040.

21. Athayde DD, Sousa BM, Dolabella ACA, Ribeiro JON, Vasconcelos DCL, Costa JCD, et al. Manufacture of highly porous tubular alumina substrates with anisotropic pore structure by freeze-casting. Adv Eng Mater. 2020;22(7):1901432. http://dx.doi.org/10.1002/adem.201901432.

22. Tang Y, Miao Q, Qiu S, Zhao K, Hu L. Novel freeze-casting fabrication of aligned lamellar porous alumina with a centrosymmetric structure. J Eur Ceram Soc. 2014;34(15):4077-82. http://dx.doi.org/10.1016/j.jeurceramsoc.2014.05.040.

23. Zhang Y, Hu L, Han J, Jiang Z. Freeze casting of aqueous alumina slurries with glycerol for porous ceramics. Ceram Int. 2010;36(2):617-21. http://dx.doi.org/10.1016/j.ceramint.2009.09.036.

24. Doremus RH. Alumina. In: Shackelford JF, Doremus RH, editors. Ceramics and glass materials: structure, properties and processing. New York: Springer; 2008. p. 1-26.

25. Said S, Mikhail S, Riad M. Recent progress in preparations and applications of meso-porous alumina. Mater Sci Energy Technol. 2019;2(2):288-97. http://dx.doi.org/10.1016/j.mset.2019.02.005.

26. Ruiz-clavijo A, Caballero-calero O, Martín-González M. Revisiting anodic alumina templates: from fabrication to applications. Nanoscale. 2021;13(4):2227-65. http://dx.doi.org/10.1039/D0NR07582E.

27. Neves TM, Pollo LD, Marcilio NR, Tessaro IC. Alumina supports produced by dry-pressing and sintering at different temperatures for developing carbon molecular sieve membranes. Ceram Int. 2021;47(22):32226-36. http://dx.doi.org/10.1016/j.ceramint.2021.08.117.

28. Queiroga JA, Nunes EHM, Souza DF, Vasconcelos DCL, Ciminelli VST, Vasconcelos WL. Microstructural investigation and performance evaluation of slip-cast alumina supports. Ceram Int. 2017;43(4):3824-30. http://dx.doi.org/10.1016/j.ceramint.2016.12.037.

29. Ray M, Bhattacharya P, Das R, Sondhi K, Ghosh S, Sarkar S. Preparation and characterization of macroporous pure alumina capillary membrane using boehmite as binder for filtration application. J Porous Mater. 2015;22(4):1043-52. http://dx.doi.org/10.1007/s10934-015-9978-9.

30. Kingery WD, Bowen HK, Uhlmann DR. Introduction to ceramics. 2nd ed. New York: Wiley; 1976.

31. Richerson DW, Lee WE. Modern ceramic engineering: properties, processing and use in design. 4th ed. Boca Raton: Taylor & Francis Group; 2018.

32. De Jonghe LC, Rahaman M. Sintering of ceramics. In: Somiya S, editor. Handbook of advanced ceramics: materials, applications, processing and properties. Oxford: Elsevier Inc.; 2003.

33. German RM. Thermodynamics of sintering. In: Fang ZZ, editor. Sintering of advanced materials. Oxford: Woodhead Publishing; 2010.

34. Lance D, Valdivieso F, Goeuriot P. Correlation between densification rate and microstructural evolution for pure alpha alumina. J Eur Ceram Soc. 2004;24(9):2749-61. http://dx.doi.org/10.1016/j.jeurceramsoc.2003.09.010.

35. Kang SJL, Jung Y. Il. Sintering kinetics at final stage sintering: model calculation and map construction. Acta Mater. 2004;52(15):4573-8. http://dx.doi.org/10.1016/j.actamat.2004.06.015.

36. Rahaman MN. Kinetics and mechanisms of densification. In: Fang ZZ, editor. Sintering of advanced materials. Oxford: Woodhead Publishing; 2010. p. 33-64.

37. Dehoff RT. Path and kinetics of microstructural change in simple sintering. In: Fang ZZ, editor. Sintering of advanced materials. Oxford: Woodhead Publishing; 2010. p. 65-85.

38. Zeng W, Gao L, Gui L, Guo J. Sintering kinetics of α-Al_2O_3 powder. Ceram Int. 1999;25(8):723-6. http://dx.doi.org/10.1016/S0272-8842(99)00008-5.

39. Kumar S, Mote VD, Prakash R, Kumar V. X-ray analysis of α-Al_2O_3 particles by Williamson-Hall methods. Mater Focus. 2016;5(6):545-9. http://dx.doi.org/10.1166/mat.2016.1345.

40. Flinn BD, Bordia RK, Zimmermann A, Rödel J. Evolution of defect size and strength of porous alumina during sintering. J Eur Ceram Soc. 2000;20(14-15):2561-8. http://dx.doi.org/10.1016/S0955-2219(00)00133-3.

41. Chakravarty D, Ramesh H, Rao TN. High strength porous alumina by spark plasma sintering. J Eur Ceram Soc. 2009;29(8):1361-9. http://dx.doi.org/10.1016/j.jeurceramsoc.2008.08.021.

42. Delbrücke T, Gouvêa RA, Moreira ML, Raubach CW, Varela JA, Longo E, et al. Sintering of porous alumina obtained by biotemplate fibers for low thermal conductivity applications. J Eur Ceram Soc. 2013;33(6):1087-92. http://dx.doi.org/10.1016/j.jeurceramsoc.2012.11.009.

43. Qin W, Peng C, Lv M, Wu J. Preparation and properties of high-purity porous alumina support at low sintering temperature. Ceram Int. 2014;40(8, Suppl 8 Pt. B):13741-6. http://dx.doi.org/10.1016/j.ceramint.2014.05.044.

44. Zheng J, Winnubst L, Velianti, Fang S, Salamon D. Manipulation of sintering behavior by initial freeze pressing an aqueous alumina suspension. Adv Eng Mater. 2011;13(1-2):77-81. http://dx.doi.org/10.1002/adem.201000199.

45. Shanti NO, Araki K, Halloran JW. Particle redistribution during dendritic solidification of particle suspensions. J Am Ceram Soc. 2006;89(8):2444-7. http://dx.doi.org/10.1111/j.1551-2916.2006.01094.x.

46. Deville S, Bernard-Granger G. Influence of surface tension, osmotic pressure and pores morphology on the densification of ice-templated ceramics. J Eur Ceram Soc. 2011;31(6):983-7. http://dx.doi.org/10.1016/j.jeurceramsoc.2010.12.021.

47. Sousa BM, Athayde DD, Vasconcelos WL. Mechanical behavior of tubular freeze-cast substrates with organized pore structure. Mater Res. 2021;24(5):e20210127. http://dx.doi.org/10.1590/1980-5373-mr-2021-0127.

48. Underwood EE. Quantitative evaluation of sectioned material. In: Elias H, editor. Stereology. Berlin: Springer; 1967.

49. ASTM: American Society for Testing and Materials. STP504-EB: stereology and quantitative metallography. West Conshohocken: ASTM; 1971.

50. Gregg SJ, Sing KSW. Adsorption, surface area and porosity. New York: Academic Press; 1982.

51. Ravikovitch PI, Haller GL, Neimark AV. Density functional theory model for calculating pore size distributions: pore structure of nanoporous catalysts. Adv Colloid Interface Sci. 1998;76-77:203-26. http://dx.doi.org/10.1016/S0001-8686(98)00047-5.

52. Cava S, Tebcherani SM, Souza IA, Pianaro SA, Paskocimas CA, Longo E, et al. Structural characterization of phase transition of Al_2O_3 nanopowders obtained by polymeric precursor method. Mater Chem Phys. 2007;103(2-3):394-9.

53. Kern A, Coelho AA, Cheary RW. Convolution based profile fitting. In: Mittemeijer E., Scardi P, editors. Diffraction analysis of the microstructure of materials. Berlin: Springer; 2004. p. 17-50.

54. Kern A. Convolution based profile fitting. In: Clearfield A, Bhuvanesh N, Reibenspies J, editors. Principles and applications of powder diffraction. Chichester: John Wiley & Sons; 2008.

55. Young RA. The Rietveld method. Oxford: Oxford University Press; 1993. 300 p. (IUCr/Oxford University Press (OUP) Book Series).

56. Grazulis S, Chateigner D, Downs RT, Yokochi AT, Quiros M, Lutterotti L, et al. Cyrstallography open database - an open-access collection of crystal structures. J Appl Cryst. 2009;42(4):726-9. http://dx.doi.org/10.1107/S0021889809016690.

57. Athayde DD, Dolabella ACA, Dias BC, Sousa BM, Silva DG, Vasconcelos DCL, et al. Production and characterization of a silica-alumina membrane using novel tubular freeze-cast substrates. Mater Res. 2019;22(2):e20180639. http://dx.doi.org/10.1590/1980-5373-mr-2018-0639.

58. Thommes M, Kaneko K, Neimark AV, Olivier JP, Rodriguez-Reinoso F, Rouquerol J, et al. Physisorption of gases with special reference to the evaluation of surface area and pore size distribution (IUPAC Technical Report). Pure Appl Chem. 2015;87(9-10):1051-69. http://dx.doi.org/10.1515/pac-2014-1117.

59. Ares JR, Pascual A, Ferrer IJ, Sánchez C. Grain and crystallite size in polycrystalline pyrite thin films. Thin Solid Films. 2005;480-481:477-81. http://dx.doi.org/10.1016/j.tsf.2004.11.064.

60. Singh LK, Bhadauria A, Jana S, Laha T. Effect of sintering temperature and heating rate on crystallite size, densification behaviour and mechanical properties of Al-MWCNT nanocomposite consolidated via spark plasma sintering. Acta Metall Sin. 2018;31(10):1019-30.